

Accounting for seismic radiation anisotropy in Bayesian survey designs

Mohamed R. Khodja¹, Michael D. Prange² and Hugues A. Djikpesse²

¹King Fahd University of Petroleum and Minerals, Center for Integrative Petroleum Research,
Dhahran, Saudi Arabia

²Schlumberger-Doll Research, Cambridge, Massachusetts, USA

Received 10 September 2014, in final form 4 January 2016

The seismic radiation patterns associated with probing the earth's subsurface are essentially anisotropic due to its ubiquitous stratified structure. This anisotropy seriously complicates formation imaging and data acquisition. This is most salient for deep-water subsalt reservoirs. Traditionally, point scatterers with isotropic radiation patterns are used in migration imaging, but in the survey design problem, these might lead to design errors caused by receivers being placed in poor locations with respect to the radiation pattern of the scattering structure. Here, we extend a framework which accounts for anisotropy in the scattered radiation for optimal geophysical survey design purposes. The propagation medium is assumed to be attenuative. The locally dipping interfaces are modeled as a discrete set of finite-size planar scattering elements. The general elastodynamic expressions for the sensitivity kernels, *i.e.*, the vectors which mathematically represent the candidate observations, in the presence of the scattering elements are provided. The size of each element controls the width of its radiation pattern, which may in turn be used to characterize the uncertainty on the dip angle, thus complementing the information provided by the model-parameter uncertainties and ultimately leading to better geophysical survey designs.

Keywords: Bayesian optimal experimental design, dipping scatterers, anisotropic radiation, layered media, model covariance matrix

1. Introduction

Optimal experimental design (OED) is a forecasting problem: one seeks to predict which experimental design will yield the best estimates of model parameters from future measurements (Chaloner and Verdinelli, 1995; Atkinson and Donev, 1992). Much work has been done in this area of research and different authors have addressed different important aspects of the problem from different perspectives (for a review of geophysical OED see the review by Maurer et al., 2010, and references therein). In particular, OED has been investigated as a

sequential augmentation problem (Wynn, 1970; Dykstra, 1971; Stummer et al., 2002, 2004; Curtis et al., 2004; Ajo-Franklin, 2009; Coles and Morgan, 2009; Guest and Curtis, 2009, 2010), from an inverse-theoretic perspective (Haber et al., 2008; Bissantz et al., 2007), and as a Bayesian statistics problem (Chaloner and Verdinelli, 1995; van den Berg et al., 2003; Sebastiani and Wynn, 2000; Clyde, 2001; Coleman and Block, 2007; Chaloner and Larntz, 1989). OED has also been applied, among other areas, to waveform inversion (Moldoveanu et al., 2013; Maurer et al., 2009; Gouveia and Scales, 1997, 1998; Rao et al., 2006; Tarantola, 1988; Virieux and Operto, 2009).

To complement the extensive work done in this area, we have proposed an efficient Bayesian greedy OED algorithm (Khodja et al., 2010) that aims to construct an experiment by sequentially minimizing the determinant of the forecast posterior model covariance matrix, *i.e.*, by maximizing the posterior Shannon information on the model. This design methodology not only takes advantage of the available prior information both on the model and on the data, but it also allows the treatment of large OED problems. This methodology has also been applied to the optimal maximization of model-parameter resolution for waveform imaging purposes (Djikpesse et al., 2012a). The benefits of the proposed method include the ability to account for source frequency bandwidth in the presence of poor signal-to-noise ratio due to attenuation. The model inhomogeneities to be imaged were modeled as a discrete set of point scatterers.

This stragghiforward approach inevitably leads to a significant problem: The elastic radiation emanating from such scatterers is essentially *isotropic* while the stratified structure of the earth's subsurface often gives rise to inhomogeneities for which scattering radiation is generally anisotropic (Kenneth, 1983). It is true that the spatial density of the point scatterers could be made large enough to model any complex structure, but no matter how fine the scattering-elements grid is, the isotropic nature of the scattered radiation could cause the design algorithm to suggest receiver locations where no radiation is forecast. This is, for instance, the case for most subsalt reservoirs, which are characterized by steep dipping interfaces on which scattering radiation is typically anisotropic which seriously complicates formation imaging and data acquisition (Xiao et al., 2013; Baldock et al., 2012; Zhuo and Ting, 2011; Moldoveanu and Kapoor, 2009; Howard, 2007; Howard and Moldoveanu, 2012; Michell et al., 2006; Farmer et al., 1996). Recently, we have considered such deep-water field from offshore Gulf of Mexico from the standpoint of Bayesian OED. This field is a typical example of a challenging subsalt reservoir with steep dips lying beneath a complex salt structure. Originally, a wide azimuth (WAZ) survey was acquired over the reservoir, but the processing of the results revealed that the steep parts of the reservoir were left untouched by the survey. Illuminating those steep parts by the traditional approach (e.g., aerial acquisition) would have been too prohibitive with regard to cost (Moldoveanu and Kapoor, 2009). The inherently anisotropic nature of the scattered radiation in this case was accounted for by introducing a

discrete set of finite-size planar scattering elements in the 3D model of the field. The study resulted in an efficient design that optimally complements the WAZ survey while accounting for the steep dipping parts of the interface under consideration and the associated uncertainties. Nevertheless, for the sake of simplicity, the study was limited to the acoustic case in the absence of attenuation.

In this article, we focus on the extension of the theoretical framework to account for seismic radiation anisotropy in Bayesian survey designs for subsurface imaging purposes. The fully elastodynamic case with attenuation is considered. Thus, the analytical expressions for the elastodynamic sensitivity kernels, *i.e.*, the rows of the sensitivity matrix, in the presence of the scattering elements will be calculated. The size of each scattering element is used to control the width of its radiation pattern, which is conveniently used to characterize the uncertainty on the dip angle, thus complementing the information provided by the model-parameter uncertainties. We start in the background section by briefly reviewing the Bayesian OED methodology we want to complement to account for radiation anisotropy, then in the next section we present the analytical expressions for the elastodynamic sensitivity kernels incorporating the design scattering elements in attenuative media. In the numerical section we present and discuss simple examples that are meant to elucidate the behavior of the design algorithm after the inclusion of the scattering elements. Finally, we summarize our results in the conclusion section.

2. Background

Here we briefly review the Bayesian design methodology presented in Khodja et al. (2010), and Dijkpessse et al. (2012a). For more details the reader is referred to these two references.

One traditional approach to optimal survey desing is based on the sensitivity matrix. The rows of the sensitivity matrix represent candidate observations and each collection of candidate observations represents a candidate experiment. Once the optimal design criterion has been defined, the collection of candidate observations that satisfy it represents an optimal experiment. We wish to find an experiment that is likely to provide information about the model parameters that will optimally complement the prior information. In particular, for a system linearized around an informative prior mean model, our goal is to find the obervations represented by the optimal acquisition vectors defined as

$$\xi_{opt} \equiv \arg \max_{\xi \in \Xi} \frac{\det(\mathbf{C})}{\det(\tilde{\mathbf{C}})}, \quad \text{for a fixed } |\Xi|, \quad (1)$$

wherein \mathbf{C} is the prior model covariance matrix, $\tilde{\mathbf{C}}$ is the posterior model covariance matrix, Ξ is the set of all possible acquisition settings, and where $|\cdot|$ stands

for the cardinal and $\det(\cdot)$ for the determinant. An experiment obtained by means of this D -optimality criterion also maximizes the trace of the model resolution matrix.

For uncorrelated data noise Eq. (1) reduces to the simple iterative expression

$$\xi_{opt}^{(n)} = \arg \max_{\xi \in \Xi} \|\gamma_{n+1}\|_{\mathbf{C}_n^*}^2, \quad \text{for a fixed } |\Xi|, \quad (2)$$

where $\gamma_{n+1} \equiv \sigma_{n+1}^{-1} \mathbf{g}_{n+1}$, σ_{n+1} being the data standard deviation and \mathbf{g}_{n+1}^T the sensitivity kernel of a candidate observation (*i.e.*, a row in the sensitivity matrix). The \mathbf{C}^* -norm is defined as, $\|\gamma_{n+1}\|_{\mathbf{C}_n^*}^2 \equiv \gamma_{n+1}^H \mathbf{C}_n^* \gamma_{n+1}$, where H stands for the Hermitian conjugate and $*$ for the complex conjugate.

Let $V \subset R^3$ be a semi-infinite domain of interest in the earth's subsurface which is bounded by a closed surface $\mathcal{S} = \mathcal{S}_0 \cup \mathcal{S}_\infty$, where \mathcal{S}_0 is a traction-free surface and \mathcal{S}_∞ is a surface at infinity where the radiation condition holds. The domain of interest V is assumed to be characterized by a generally spatially varying mass density, $\rho(\mathbf{x})$, and stiffness coefficients, $c_{ijkl}(\mathbf{x})$, where \mathbf{x} is the position vector in a Cartesian coordinate system. The stiffness coefficients are assumed to be complex quantities that satisfy the usual symmetries $c_{ijkl}(\mathbf{x}) = c_{jikl}(\mathbf{x}) = c_{klij}(\mathbf{x}) = c_{ijlk}(\mathbf{x})$ and whose imaginary parts are responsible for the attenuation of propagating elastic waves (Toksöz and Johnson, 1981; Zhu and Tsvankin, 2006). The preceding symmetry relations reduce the rank-four stiffness tensor to a 6×6 matrix that has only 21 independent elements, in the most general case.

In the frequency domain, the general equation governing elastodynamic phenomena can be written as

$$\omega^2 \rho(\mathbf{x}) u_i(\mathbf{x}, \omega) + \sum_{j,k,l} \partial_j [c_{ijkl}(\mathbf{x}) \partial_k u_l(\mathbf{x}, \omega)] = s_i(\mathbf{x}, \omega), \quad (3)$$

where $u_i(\mathbf{x}, \omega)$ is the i^{th} component of displacement at point $\mathbf{x} \in V$ and frequency ω , $\partial_j \equiv \partial / \partial x_j$, and $s_i(\mathbf{x}, \omega)$ the source term. This source term is defined in terms of the volume density of force $f_i(\mathbf{x}, \omega)$ and the volume density of moment $T_{ij}(\mathbf{x}, \omega)$ as

$$s_i(\mathbf{x}, \omega) \equiv f_i(\mathbf{x}, \omega) + \sum_j \partial_j T_{ij}(\mathbf{x}, \omega). \quad (4)$$

The solution of Eq. (3) may be expressed as a function of the outgoing Green's function $\mathcal{G}_{in}(\mathbf{x}, \mathbf{x}', \omega)$ as (Aki and Richards, 2002)

$$u_i(\mathbf{x}, \omega) = - \int_V \sum_j \mathcal{G}_{ij}(\mathbf{x}, \mathbf{x}', \omega) s_j(\mathbf{x}', \omega) d^3 \mathbf{x}'. \quad (5)$$

Now, let us assume that the propagation medium represented by the vector $\mathbf{m}(\mathbf{x}) \equiv (\rho(\mathbf{x}), \{c_{ijkl}(\mathbf{x})\})$ may be viewed as the superposition of a reference medium represented by the vector $\mathbf{m}^{(0)}(\mathbf{x}) \equiv (\rho^{(0)}(\mathbf{x}), \{c_{ijkl}^{(0)}(\mathbf{x})\})$ and a perturbation model represented by the vector $\Delta\mathbf{m}(\mathbf{x}) \equiv (\Delta\rho(\mathbf{x}), \{\Delta c_{ijkl}(\mathbf{x})\})$ so that

$$\left. \begin{aligned} \rho(\mathbf{x}) &= \rho^{(0)}(\mathbf{x}) + \Delta\rho(\mathbf{x}), \\ c_{ijkl}(\mathbf{x}) &= c_{ijkl}^{(0)}(\mathbf{x}) + \Delta c_{ijkl}(\mathbf{x}). \end{aligned} \right\} \quad (6)$$

Under the Born approximation the scattered displacement fields can be written as

$$\begin{aligned} \Delta u_i(\mathbf{x}, \omega) &= \omega^2 \int_V \sum_j \mathcal{G}_{ij}^{(0)}(\mathbf{x}, \mathbf{x}', \omega) u_j^{(0)}(\mathbf{x}', \omega) \Delta\rho(\mathbf{x}') d^3\mathbf{x}' - \\ &\quad - \int_V \sum_{j,k,l,n} \partial'_k [\mathcal{G}_{in}^{(0)}(\mathbf{x}, \mathbf{x}', \omega)] \Delta c_{nkij}(\mathbf{x}') \partial'_l u_j^{(0)}(\mathbf{x}', \omega) d^3\mathbf{x}', \end{aligned} \quad (7)$$

wherein $\mathcal{G}_{in}^{(0)}(\mathbf{x}, \mathbf{x}', \omega)$ is the outgoing Green's function in the unperturbed medium and $u_i^{(0)}(\mathbf{x}', \omega)$ is the unperturbed field in the reference medium given by

$$u_i^{(0)}(\mathbf{x}, \omega) = - \int_V \sum_j \mathcal{G}_{ij}^{(0)}(\mathbf{x}, \mathbf{x}', \omega) s_j(\mathbf{x}', \omega) d^3\mathbf{x}' \quad (8)$$

Note that in writing Eq. (7) we have not assumed any particular source type nor have we assumed any particular structure for the inhomogeneities in the propagation medium (within the limits imposed by the Born approximation). Now, we wish to restrict Eq. (7) by assuming that the inhomogeneities are in fact a discrete set of one-dimensional or two-dimensional scattering elements.

3. Scattering elements for design purposes

In this section, we derive the general expressions for the elastodynamic sensitivity kernels, *i.e.*, the vectors which mathematically represent the candidate observations, in the presence of the scattering elements. The propagation medium is assumed to be attenuative and the locally dipping interfaces are modeled as a discrete set of finite-size planar scattering elements. We also discuss how the size of each element controls the width of its radiation pattern, which may in turn be used to characterize the uncertainty on the dip angle, thus complementing the information provided by the model-parameter uncertainties and ultimately leading to better geophysical survey designs.

For our survey design purposes it is sufficient to assume that the contrasts in elastic parameters are constant over the extent of the individual scattering elements, although they may vary from one element to another. Thus, the scattering potentials corresponding to M scattering elements with constant contrasts $\Delta\rho_\beta$ and $(\Delta c_{ijkl})_\beta$, $\beta = 1, 2$, are given by

$$\left. \begin{aligned} \Delta\rho(\mathbf{x}) &= \sum_{\beta=1}^M \Delta\rho_\beta \psi_\beta^{(D)}(\mathbf{x}), \\ \Delta c_{ijkl}(\mathbf{x}) &= \sum_{\beta=1}^{(6 \times 6)M} (\Delta c_{ijkl})_\beta \psi_\beta^{(D)}(\mathbf{x}), \end{aligned} \right\} \quad (9)$$

wherein $\psi_\beta^{(D)}$ the 's are indicator functions that encode the shape of the scattering elements. According to Huygens's principle, a D -dimensional scatterer $\mathcal{A}_\beta^{(D)}$, $D = 1, 2$, may be viewed as consisting of a continuous set of point scatterers. Thus, the form factors may be defined as

$$\psi_\beta^{(D)}(\mathbf{x}) \equiv \int_{\mathcal{A}_\beta^{(D)}} \delta(\mathbf{x} - \mathbf{y}_\beta(\Lambda^{(D)})) d\Lambda^{(D)}, \quad (10)$$

where $\delta(\cdot)$ stands for the Dirac delta and $\Lambda^{(D)}$ stands for the set of integration parameters that characterize the spatial extent of the scattering elements. For a line-segment $\mathcal{A}_\beta^{(1)}$, $\Lambda^{(1)}$ is merely a real number while, when the scattering elements are two-dimensional disks $\mathcal{A}_\beta^{(2)}$, $\Lambda^{(2)}$ takes on the form of a pair of real numbers: the first one spans the radial extent of the disks and the second one represents their sweeping angle (*i.e.*, $\Lambda^{(2)} \equiv (\nu, \phi) \in [0, 1] \times [0, 2\pi]$, for instance). Substituting Eq. (10) into Eqs. (7) and taking into account the definition of $\psi_\beta^{(D)}(\mathbf{x})$ yields

$$\begin{aligned} \Delta u_i(\mathbf{x}, \omega) &= \sum_{\beta=1}^M \omega^2 \Delta\rho_\beta \int_{\mathcal{A}_\beta^{(D)}} \sum_j \mathcal{G}_{ij}^{(0)}(\mathbf{x}, \mathbf{y}_\beta(\Lambda^{(D)}), \omega) u_j^{(0)}(\mathbf{y}_\beta(\Lambda^{(D)}), \omega) d\Lambda^{(D)} - \\ &\quad - \sum_{\beta=1}^M \int_{\mathcal{A}_\beta^{(D)}} \sum_{j,k,l,n} (\Delta c_{nklij})_\beta \left[\partial'_k \mathcal{G}_{in}^{(0)}(\mathbf{x}, \mathbf{x}', \omega) \partial'_l u_j^{(0)}(\mathbf{x}', \omega) \right]_{\mathbf{x}'=\mathbf{y}_\beta(\Lambda^{(D)})} d\Lambda^{(D)}. \end{aligned} \quad (11)$$

This equation may be written concisely as

$$\Delta u_i \equiv \sum_{\beta=1}^{(1+6 \times 6)M} G_{i\beta} \Delta m_\beta, \quad (12)$$

where $\{\Delta m_\beta\}_{1 \leq \beta \leq M}$ are the mass density contrasts, $\{\Delta m_\beta\}_{M+1 \leq \beta \leq (6 \times 6)M}$ are the stiffness contrasts, and $G_{i\beta}$ are the entries of a possibly complex $N \times (1 + 6 \times 6)M$ sensitivity matrix. N and $(1 + 6 \times 6)M$ are the number of displacement observations and the number of model parameters, respectively. The entries of the sensitivity matrix, $G_{i\beta}$, can be split into two categories: entries $G_{i\beta}^{(\rho)}$, which represent the contributions associated with the mass density contrasts $\Delta\rho_\beta$, and $G_{i\beta}^{(c)}$ which represent the contributions associated with the stiffness contrasts $(\Delta c_{nkij})_\beta$. They are given by

$$\left. \begin{aligned} G_{i\beta}^{(\rho)} &\equiv \omega^2 \int_{A_\beta^{(D)}} \sum_j G_{ij}^{(0)}(\mathbf{x}, \mathbf{y}_\beta(\Lambda^{(D)}), \omega) u_j^{(0)}(\mathbf{y}_\beta(\Lambda^{(D)}), \omega) d\Lambda^{(D)} \\ G_{i\beta}^{(c)} &\equiv - \int_{A_\beta^{(D)}} \left[\partial'_k G_{in}^{(0)}(\mathbf{x}, \mathbf{x}', \omega) \partial'_l u_j^{(0)}(\mathbf{x}', \omega) \right]_{\mathbf{x}'=\mathbf{y}_\beta(\Lambda^{(D)})} d\Lambda^{(D)}. \end{aligned} \right\} \quad (13)$$

The explicit calculation of these matrix entries for simple cases (see appendices A and B) shows that the introduction of a spatial extent for the scattering elements manifests itself as an overall factor that multiplies the matrix entries of the point-scatterers case. This factor reduces to unity when the spatial extent vanishes and reproduces the effects of specular reflection when the spatial extent is much larger than the wavelength of the wave (see, *e.g.*, Eqs. (25) and (26)). Thus, the spatial extent of the scattering structures could be used as a controllable parameter to characterize the uncertainty on the structural dip – a higher confidence in the dipping character of the scattering structures would translate into larger sizes for the scattering structures, thereby making the scattering more specular. For instance, in the 2D acoustic example discussed in appendix A a heuristic rule of thumb could be

$$l \sim \phi^{-1} \sim \sigma_{dip}^{-1} \quad (14)$$

where l is the length of the line-segment scatterer, ϕ is a measure of the beam width which could be, for instance, the half-power beamwidth (HPBW) or the first-null beamwidth (FNBW) (Balanis, 2005), and σ_{dip} is the dip-angle standard deviation. Let us identify ϕ with σ_{dip} . Introducing the normalized length $0 \leq \bar{l} \equiv l/\lambda < \infty$ and the normalized standard deviation $0 \leq \bar{\sigma}_{dip} \equiv \sigma_{dip}/\pi \leq 1$, one can devise another simple expression that is more quantitatively meaningful than Eq. (14) and which has the correct asymptotic behavior, namely

$$\bar{l} \equiv \frac{1}{\bar{\sigma}_{dip}} - 1. \quad (15)$$

Given a particular uncertainty on the dip, $\bar{\sigma}_{dip}$, Eq. (15) allows us to calculate the size of the scattering elements.

4. Numerical examples

We now present and discuss a set of simple synthetic examples whose purpose is to elucidate the behavior of the OED algorithm after the scattering elements have been incorporated into it in an elastic attenuative setting.

In the first part of this study, we start by reviewing the acoustic case to clarify additional aspects of the augmented algorithm. Our goal is to show how the OED algorithm reacts to the presence of scattered anisotropic acoustic radiation in a simple 2D model with line-segment scatterers. The particular dip-angle model of the line-segment scatterers is assumed to be based on prior information. The algorithm is expected to react to the presence of anisotropic radiation by suggesting surveys where receivers are placed where scattered radiation is forecast.

Consider a 2D homogeneous reference model with velocity 2500 m/s. A 20×20 array of point scatterers is superimposed on this model with a vertical and horizontal spacing of 15 m (Fig. 1a). The experimental setup consists of one source at the top center of the model and 295 receivers uniformly distributed around the model with a separation of 10 m. The prior model covariance matrix is assumed to be $\mathbf{C} = (2 \times 10^{-4})^2 \mathbf{I}$ and the data covariance matrix is taken to be $\mathbf{C}_D = (10^{-3} \mu\text{Pa})^2 \mathbf{I}$, which is consistent with a noise level of 20% for a uniform scattering strength $\Delta m = 10^{-3}$ (see definition in Eq. (21)).

The results of the simulations are shown in Figs. 1b–1e. In Figs. 1b and 1c we show the best designs for 30 and 50 observations, respectively, suggested by the OED algorithm when the scattering elements are assumed to be point structures. In Figs. 1d and 1e we show the corresponding designs for horizontal scattering elements with $l = 20$ wavelengths. The wave emitted from each source interacts with all scatterers and the data collected at each receiver is the combined result of this interaction. Thus, the curves connecting sources and receivers in Figure 1 do not represent actual ray-paths; they are just a convenient way of showing which source-receiver pairs have been selected in the design. Also, note that n observations do not generally correspond to n unique source-receiver pairs. This is because the design might repeat observations in order to suppress anticipated noise.

In Figs. 1d and 1e, the extended line scatterers cause specular reflection and transmission to dominate. The algorithm avoids suggesting receiver locations where there is no scattered radiation or where this radiation is weak. This is to be contrasted with the survey depicted in Figs. 1b and 1c where the scattering elements are pointlike. There, the isotropic nature of the scattered radiation allows the algorithm to suggest observations that optimally reduce the model uncertainties by selecting more receiver locations along the sides of the model.

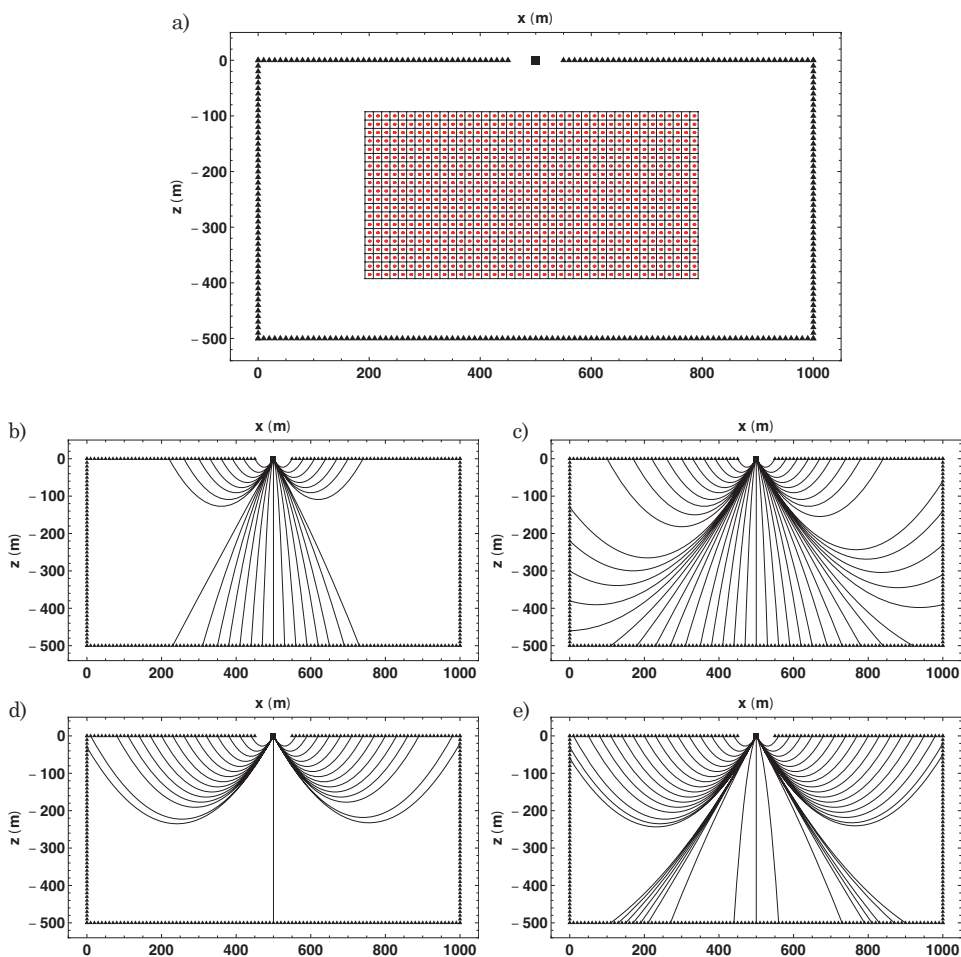


Figure 1. 2D homogeneous reference model. (a) The experimental setup used to illustrate the main results. The red dots represent the scattering elements and the squares of the grid represent the model parameters. (b), (c) The first best 30 and 50 observations, respectively, suggested by the OED algorithm when the scattering elements are point structures. (d), (e) The first best 30 and 50 observations, respectively, suggested by the OED algorithm when the scattering elements are line-segments. The curves are not actual ray-paths, they are just meant to show which source-receiver pair was selected.

The reason the OED algorithm appears to first favor observations for the line scatterers that correspond to receivers located on the top of the model is illustrated in Fig. 2. The reflected waves reinforce each other at the receivers located along the top of the model, providing more information on the scattering potential from each of these scatterers. Transmitted waves interact with fewer scatterers and thus provide less information than the reflected waves. Furthermore, for

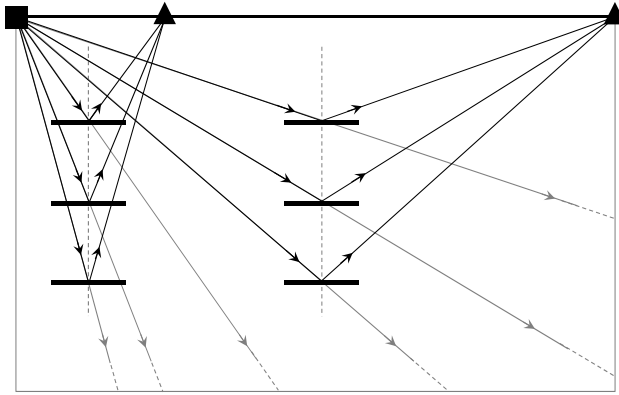


Figure 2. What happens when the scatterers are large enough for specular reflection to take place? Illustration of the basic physical process responsible for the favoring by the OED algorithm of receivers collecting reflected radiation over receivers collecting transmitted radiation when the scatterers are large enough for specular reflection to take place. This is essentially the reason the observations that correspond to receivers on the surface were selected first in the example depicted in Figs. 1d and 1e.

reflected waves the algorithm preferentially selects receivers that are closer to the source because geometrical spreading would attribute these with higher signal-to-noise ratios.

To see how the algorithm behaves in the presence of attenuation, we show in Fig. 3 the design corresponding to the first best 55 observations in the simple

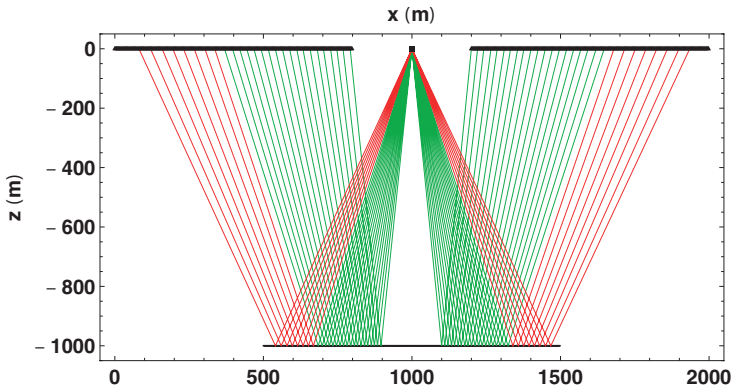


Figure 3. The effect of attenuation. The first best 55 observations when an attenuation factor of $Q = 75$ is assumed. The line at the bottom represents the location of the line-segment scatterers with individual lengths $l = 7,000$ m. The different colors of the curved lines showing the source-receiver pairs encode the wavelengths corresponding to the selected observations: purple ($\lambda = 50$ m), blue ($\lambda = 100$ m), green ($\lambda = 150$ m), and red ($\lambda = 200$ m). There are no purple or blue curves.

situation when the scattering elements are a single row of line-segments of length $l = 10^3$ m. Four wavelengths were used $\lambda = 50, 100, 150,$ and 200 m and the attenuation factor was assumed to be $Q = 75$ (see Xu and Stewart (2006) for comparison). The algorithm rendered a design which was a mix of different frequencies which clearly represents a trade-off between frequency and offset. The algorithm starts by selecting the receivers that correspond to the minimum offset, *i.e.*, those that are closer to the source, using the 150-m waves. Afterwards, when balancing wavelength (frequency) and offset favors a longer wavelength, the algorithm selects observations that correspond to the 200-m waves. Note that the algorithm exhibits a maximum threshold in the used frequencies. This is a desirable feature that allows the designer to use less costly sources (*e.g.*, lower frequencies) while not compromising the quality of the survey.

5. Conclusion

The use of point scatterers to model the stratified structure of the earth's subsurface is inherently marred by the isotropic nature of the radiation scattered from these point structures and could cause the surveys to have receiver locations where no radiation is forecast. Here, we have augmented a Bayesian methodology for designing seismic surveys to address this issue. The locally dipping interfaces have been modeled as a discrete set of one-dimensional and two-dimensional scattering, or design, elements. We have provided the general formulas giving the entries of the design matrix that incorporates those elements. To account for prior information on model dips, we have also used the sizes of these design elements to characterize the uncertainty on the dip angle thus complementing the information provided by the model-parameter uncertainties leading to better survey designs. We have illustrated our main results with simple numerical examples.

Acknowledgments – MRK gratefully acknowledges the support of Schlumberger-Doll Research, where most of this work has been done, and King Fahd University of Petroleum and Minerals.

References

- Atkinson, A. C. and Donev, A. N. (1992): *Experimental Designs*. Oxford Statistical Science Series 8, Oxford Science Publications, Clarendon Press, Oxford, UK, 352 pp, ISBN 10: 0198522541 / ISBN 13: 9780198522546.
- Ajo-Franklin, J. B. (2009): Optimal experiment design for time-lapse traveltime tomography, *Geophysics*, 74(4), Q27–Q40, DOI: 10.1190/1.3141738.
- Aki, K. and Richards, P. G. (2002): *Quantitative Seismology*. 2nd Edition, University Science Books, Sausalito, CA, USA, 700 pp.
- Balanis, C. (2005): *Antenna Theory: Analysis, and Design*. 3rd Edition, John Wiley and Sons, Hoboken, NJ, USA, 94–96.

- Baldock, S., Reta-Tang, C., Beck, B., Gao, W., Cai, J. and Hightower, S. (2012): Orthogonal wide azimuth surveys: Acquisition and imaging, *First Break*, **30**(9), 147–151, DOI: [10.3997/1365-2397.2012012](https://doi.org/10.3997/1365-2397.2012012).
- Ben-Menahem, A. and Singh, S. J. (1981): *Seismic Waves and Sources*, Springer-Verlag, New York, NY, USA, 1108 pp, ISBN: 978-1-4612-5856-8.
- Beylkin, G. (1985): Imaging of discontinuities in the inverse scattering problem by inversion of a causal generalized Radon transform, *J. Math. Phys.*, **26**, 99–108, DOI: [10.1063/1.526755](https://doi.org/10.1063/1.526755).
- Bissantz, N., Hohage, T., Munk, A. and Ruymgaart, F. (2007): Convergence rates of general regularization methods for statistical inverse problems and applications, *SIAM J. Numer. Anal.*, **45**, 2610–2636, DOI: [10.1137/060651884](https://doi.org/10.1137/060651884).
- Chaloner, K. and Larntz, K. (1989): Optimal Bayesian designs applied to logistic regression experiments, *J. Stat. Plan. Inference*, **21**, 191–208, DOI: [10.1016/0378-3758\(89\)90004-9](https://doi.org/10.1016/0378-3758(89)90004-9).
- Chaloner, K. and Verdinelli, I. (1995): Bayesian experimental design: A review, *Statistical Science*, **10**, 273–304.
- Clyde, M. (2001): Experimental design: A Bayesian perspective, in: *International Encyclopedia of the Social and Behavioral Sciences*. Elsevier Science Ltd, Oxford, UK, 5075–5081.
- Coleman, M. C. and Block, D. E. (2007): Nonlinear experimental design using Bayesian regularization neural networks, *AICHE J.*, **53**, 1496–1509, DOI: [10.1002/aic.11175](https://doi.org/10.1002/aic.11175).
- Coles, D. A. and Morgan, F. D. (2009): A method for fast, sequential experimental design for linearized geophysical inverse problems, *Geophys. J. Int.*, **178**, 145–158, DOI: [10.1111/j.1365-246X.2009.04156.x](https://doi.org/10.1111/j.1365-246X.2009.04156.x).
- Curtis, A., Michelini, A., Leslie, D. and Lomax, A. (2004): A deterministic algorithm for experimental design applied to tomographic and microseismic monitoring surveys, *Geophys. J. Int.*, **157**, 595–606, DOI: [10.1111/j.1365-246x.2004.02114.x](https://doi.org/10.1111/j.1365-246x.2004.02114.x).
- Djikpesse, H. A., Khodja, M. R., Prange, M. D., Duchenne, S. and Menkiti, H. (2012a): Bayesian survey design to optimize resolution in waveform inversion, *Geophysics*, **77**(22), 81–93, DOI: [10.1190/geo2011-0143.1](https://doi.org/10.1190/geo2011-0143.1).
- Djikpesse, H. A., Prange, M. D., Khodja, M. R., Duchenne, S. and Moldoveanu, N. (2012b): Subsalt optimal survey design with dipping scatterers, in: *74th EAGE Conference*, Copenhagen, Denmark, 4–7 June 2012, DOI: [10.3997/2214-4609.20148383](https://doi.org/10.3997/2214-4609.20148383).
- Dykstra, O. (1971): The augmentation of experimental data to maximize $|XX|$, *Technometrics*, **13**, 682–688, DOI: [10.2307/1267180](https://doi.org/10.2307/1267180).
- Farmer, P., Miller, D., Pieprzak, A., Rutledge, J. and Woods, R. (1996): Exploring the subsalt, *Oilfield Review*, **8**, 50–64.
- Gouveia, W. P. and Scales, J. A. (1997): Resolution of seismic waveform inversion: Bayes versus Occam, *Inverse Problems*, **13**, 323–349.
- Gouveia, W. P. and Scales, J. A. (1998): Bayesian seismic waveform inversion: Parameter estimation and uncertainty analysis, *J. Geophys. Res.*, **103**, 2759–2779, DOI: [10.1029/97JB02933](https://doi.org/10.1029/97JB02933).
- Guest, T. and Curtis, A. (2009): Iteratively constructive sequential design of experiments and surveys with nonlinear parameter-data relationships, *J. Geophys. Res.*, **114**, B04307, DOI: [10.1029/2008JB005948](https://doi.org/10.1029/2008JB005948).
- Guest, T. and Curtis, A. (2010) Optimal trace selection for AVA processing of shale-sand reservoirs, *Geophysics*, **75**(4), C37–C47, DOI: [10.1190/1.3462291](https://doi.org/10.1190/1.3462291).
- Haber, E., Horesh, L. and Tenorio, L. (2008): Numerical methods for experimental design of large-scale linear ill-posed inverse problems, *Inverse Problems*, **24**, 055012.
- Howard, M. S. (2007): Marine seismic surveys with enhanced azimuth coverage: Lessons in survey design and acquisition, *The Leading Edge*, **26**(4), 480–493, DOI: [10.1190/1.2723212](https://doi.org/10.1190/1.2723212).

- Howard, M. S. and Moldoveanu, N. (2012): Marine survey design for rich-azimuth seismic using surface streamers, in: *SEG Technical Program Expanded Abstracts*, 2915–2919, DOI: [10.1190/1.2370132](https://doi.org/10.1190/1.2370132).
- Kenneth, B. L. N. (1983): *Seismic Wave Propagation in Stratified Media*. Cambridge University Press, Cambridge, UK, 242 pp.
- Khodja, M. R., Prange, M. D. and Djikpesse, H. A. (2010): Guided Bayesian optimal experimental design, *Inverse Problems*, **26**, 055008.
- Khodja, M. R., Prange, M. D. and Djikpesse, H. A. (2012): A heuristic Bayesian design criterion for imaging resolution enhancement, in: *Proceedings of the 2012 IEEE Statistical Signal Processing Workshop*, 9–12, DOI:[10.1109/SSP.2012.6319862](https://doi.org/10.1109/SSP.2012.6319862).
- Maurer, H. R., Curtis, A. and Boerner, E. (2010): Recent advances in optimized geophysical survey design, *Geophysics*, **75**(5), 75A177–75A194, DOI:[10.1190/1.3484194](https://doi.org/10.1190/1.3484194).
- Maurer, H. R., Greenhalgh, S. A. and Latzel, S. (2009): Frequency and spatial sampling strategies for frequency-domain cross-hole experiments optimized design of frequency-domain acoustic waveform tomography experiments, *Geophysics*, **74**(6), WCC11–WCC21, DOI: [10.1190/1.3157252](https://doi.org/10.1190/1.3157252).
- Michell, S., Shoshitaishvili, E., Chergotis, D., Sharp, J. and Etgen, J. (2006): Wide azimuth streamer imaging of mad dog: Have we solved the subsalt imaging problem? in: *Proceedings of the 76th SEG Annual Meeting Conference*, 1-6 October 2006, New Orleans, Louisiana, USA, 2905–2909.
- Miller, D., Oristaglio, M. and Beylkin, G. (1987): A new slant on seismic imaging: migration and integral geometry, *Geophysics*, **52**(7), 943–964, DOI: [10.1190/1.1442364](https://doi.org/10.1190/1.1442364).
- Moldoveanu, N. and Kapoor, J. (2009): What is the next step after WAZ for exploration in the Gulf of Mexico? In: *Proceedings of the 79th SEG Annual Meeting Conference*, 25-30 October 2009, Houston, Texas, USA, 41–45.
- Moldoveanu, N., Fletcher, R., Lichnewsky, A. and Coles, D. (2013): New aspects in seismic survey design, in: *SEG Technical Program Expanded Abstracts 2013*, 186–190, DOI: [10.1190/segam2013-0668.1](https://doi.org/10.1190/segam2013-0668.1).
- Rao, Y., Wang, Y. and Morgan, J. V. (2006): Crosshole seismic waveform tomography - II. Resolution analysis. *Geophys. J. Int.*, **166**, 1237–1248, DOI: [10.1111/j.1365-246X.2006.03031.x](https://doi.org/10.1111/j.1365-246X.2006.03031.x).
- Sebastiani P. and Wynn, H. P. (2000): Maximum entropy sampling and optimal Bayesian experimental design, *J. Roy. Stat. Soc.*, **B62**, 145–157, DOI: [10.1111/1467-9868.00225](https://doi.org/10.1111/1467-9868.00225).
- Snieder, R. (2002): General theory of elastic wave scattering, in: *Scattering and Inverse Scattering in Pure and Applied Science*, edited by Pike, R. and Sabatier, P., Academic Press, San Diego, CA, USA, 528–542.
- Stummer, P., Maurer, H., Horstmeyer, H. and Green, A. G. (2002): Optimization of DC resistivity data acquisition: Real-time experimental design and a new multielectrode system, *IEEE Trans. Geosci. Remote Sens.*, **40**, 2727–2735.
- Stummer, P., Maurer, H. and Green, A. G. (2004): Experimental design: Electrical resistivity data sets that provide optimum subsurface information, *Geophysics*, **69**, 120–139, DOI: [10.1190/1.1649381](https://doi.org/10.1190/1.1649381).
- Tarantola, A. (1988): Theoretical background for the inversion of seismic waveforms, including elasticity and attenuation, *Pure Appl. Geophys.*, **128**, 365–399, DOI: [10.1007/BF01772605](https://doi.org/10.1007/BF01772605).
- Toksöz, M. N. and Johnson, D. H. (1981): *Seismic Wave Attenuation (Geophysics Reprint Series - No. 2.)* Society of Exploration Geophysicists, Tulsa, OK, USA, ISBN 10: 0931830168 / ISBN 13: 978-0931830167.
- Van Den Berg, J., Curtis, A. and Trampert, J. (2003): Optimal nonlinear Bayesian design: An application to amplitude versus offset experiments, *Geophys. J. Int.*, **155**, 411–421, DOI: [10.1046/j.1365-246X.2003.02048.x](https://doi.org/10.1046/j.1365-246X.2003.02048.x).

- Virieux, J. and Operto, S. (2009): An overview of full-waveform inversion in exploration geophysics, *Geophysics*, **74**(6), WCC127-WCC152, DOI: [10.1190/1.3238367](https://doi.org/10.1190/1.3238367).
- Wynn, H. P. (1970): The sequential generation of D-optimum experimental designs, *Ann. Math. Statist.*, **41**, 1655–1664.
- Xiao, X., He, Y., Gersztenkorn, A., Yang, S. and Wang, B. (2013): Orthorhombic imaging for orthogonal wide azimuth surveys in Mississippi canyon, Gulf of Mexico, in: *75th EAGE Conference and Exhibition*, London, UK, 10–13 June 2013, available at http://www.searchanddiscovery.com/pdfz/documents/2014/30391he/ndx_he.pdf.html
- Xu, C. and Stewart, R. R. (2006): Estimating seismic attenuation (Q) from VSP data, *CSEG Recorder*, **31**, 57–61.
- Zhu, Y. and Tsvankin, I. (2006): Plane-wave propagation in attenuative transversely isotropic media. *Geophysics*, **128**(2), T17–T30, DOI: [10.1190/1.2187792](https://doi.org/10.1190/1.2187792).
- Zhuo, L. and Ting, C.-O. (2011): Subsalt steep dip imaging study with 3D acoustic modeling, in: *73rd EAGE Conference and Exhibition incorporating SPE EUROPEC 2011*, Vienna, Austria, 23–26 May 2011, available at http://www.cgg.com/technicalDocuments/cggv_0000010603.pdf

SAŽETAK

Proračun za anizotropiju seizmičkog zračenja kod dizajna istraživanja u Bayesovom smislu

Mohamed R. Khodja, Michael D. Prange i Hugues A. Djikpesse

Prostorna razdioba seizmičkog zračenja koje se koristi za proučavanje unutrašnjosti Zemlje je anizotropna zbog Zemljine slojevite građe. Ta anizotropija znatno komplicira razlučivanje struktura i prikupljanje podataka, što je najizraženije pri istraživanju podzemskih nalazišta ispod solnih naslaga. Korištenje točkastih raspršivača s izotropnom razdiobom zračenja, koji se tradicionalno koriste u prospekciji, može dovesti do ozbiljnih pogrešaka ako se pri planiranju istraživanja prijemnici postave na neodgovarajuće pozicije u odnosu na razdiobu zračenja istraživane strukture. U ovom radu razrađujemo optimalni sustav kojim se raspršeno zračenje može uzeti u obzir pri planiranju istraživanja. Sredstvo kroz koje se rasprostiru valovi je atenuativno, a lokalno nagnute granice među slojevima su modelirane diskretnim skupom plošnih raspršivača konačne veličine. Prikazane su opće elastodinamičke jednadžbe za kernele razlučivosti, tj. za vektore koji matematički prikazuju moguća opažanja ako postoje raspršivači. Veličina pojedinog raspršivača određuje širinu njegove razdiobe zračenja kojom se može izraziti nepouzdanost kuta nagiba plohe, što daje dodatne informacije o nepouzdanostima parametara modela, te u konačnici vodi boljem planiranju geofizičkih istraživanja.

Ključne riječi: optimalan dizajn istraživanja u Bayesovom smislu, nagnuti raspršivači, anizotropna radijacija, slojevito sredstvo, kovarianca parametara modela

Corresponding author's address: Dr. Mohamed R. Khodja, King Fahd University of Petroleum and Minerals, Center for Integrative Petroleum Research, Dhahran 31261, Saudi Arabia; e-mail: mrkhodja@kfupm.edu.sa

Appendix A. Two-dimensional acoustic survey designs

In this appendix we calculate the sensitivity kernels associated with 1D scattering elements to see how their expressions differ from the sensitivity kernels associated with the isotropic point-scatterer case. The equation governing the propagation of the P-waves takes on the form

$$\left[\nabla^2 + K^2(\mathbf{x}, \omega) + \frac{\omega^2}{c^2(\mathbf{x})} q(\mathbf{x}) \right] p(\mathbf{x}, \omega) = \phi(\mathbf{x}, \omega), \quad (16)$$

where we have defined the complex propagation constant

$$K^2(\mathbf{x}, \omega) \equiv \frac{\omega^2}{c^2(\mathbf{x})} \left[1 + \frac{i}{Q(\mathbf{x})} \right], \quad (17)$$

with $Q(\mathbf{x})$ being the attenuation parameter and $q(\mathbf{x})$ the dimensionless scattering potential. Let us also assume that the background velocity and the attenuation parameter Q are constant, *i.e.*, $c(\mathbf{x}) = c$ and $Q(\mathbf{x}) = Q$, and that the wave source is a point source located at $\mathbf{x}^{(s)}$. The scattered wave is recorded at a receiver located at $\mathbf{x}^{(rec)}$. The scattered pressure field is thus given by (Beylkin, 1985; Miller et al., 1987)

$$\Delta p(\mathbf{x}^{(s)}, \mathbf{x}^{(rec)}, \omega) = \left(\frac{\omega}{c} \right)^2 \int \mathcal{G}^{(0)}(\mathbf{x}^{(s)}, \mathbf{x}, \omega) \mathcal{G}^{(0)}(\mathbf{x}, \mathbf{x}^{(rec)}, \omega) q(\mathbf{x}) d^3 \mathbf{x}, \quad (18)$$

where $\mathcal{G}^{(0)}(\mathbf{x}, \mathbf{x}', \omega)$ is the background Green's function.

Let us assume that our design problem is a 2D problem. In this case we have

$$\mathcal{G}^{(0)}(\mathbf{x}, \mathbf{x}', \omega) \approx \sqrt{\frac{ic}{8\pi\omega}} \frac{e^{iK(\omega)|\mathbf{x}-\mathbf{x}'|}}{\sqrt{|\mathbf{x}-\mathbf{x}'|}}, \quad (19)$$

which is the leading term in the asymptotic expansion of the background 2D Green's function. The use of the 2D Green's functions rather than the 3D Green's functions is adopted merely for convenience. None of the main results of this study is affected by the dimensionality of the Green's functions. The main differences between the 2D and 3D kernels resides in the factor of ω versus ω^2 (Beylkin, 1985), and the different geometric spreading factors.

Consider the case of S point sources emitting waves that scatter off M regularly separated point scatterers to be recorded at R receivers. We would like to discuss the effects of adding dip angles to the scatterers. Our goal is to extend our methodology to associate radiation patterns with the scatterers used in the migration imaging problem. Traditionally, point scatterers with isotropic radiation

patterns are used in migration imaging, but in the survey design problem, these might lead to design errors caused by receivers being placed in poor locations with respect to the radiation pattern of the scattering structure. Our new approach accounts for these patterns by replacing each point scatterer by a small scattering structure (e.g. a disk in 3D or a line segment in 2D) that would yield the correct radiation pattern for the corresponding dips in the prior model. Let us first consider the case when the scatterers in a 2D model are line segments instead of point scatterers. The generalization to the 3D case where the scatterers are small reflecting disks is straightforward.

For a line-segment $\mathcal{A}_\beta^{(1)}$ whose center is located at \mathbf{a}_β , $\Lambda^{(1)} \equiv \nu \in [-1/2, 1/2]$ and

$$\mathbf{y}_\beta(\nu) = \mathbf{a}_\beta + \nu l_\beta \mathbf{u}_\beta, \quad (20)$$

where l_β is the line-segment length and \mathbf{u}_β a unit vector along its direction. This leads to the scattering potential

$$q(\mathbf{x}) = \sum_{\beta=1}^M \Delta m_\beta \int_{-1/2}^{1/2} \delta(\mathbf{x} - \mathbf{a}_\beta - \nu l_\beta \mathbf{u}_\beta) d\nu, \quad (21)$$

Now, substituting this result into Eq. (18) leads to the following expression for the sensitivity kernels

$$G_{c\beta}(\omega) = \frac{i\omega}{8\pi c} \int_{-1/2}^{1/2} \frac{e^{iK(\omega)|\mathbf{R}_\alpha^{(s)} + \nu l_\beta \mathbf{u}_\beta|}}{\sqrt{|\mathbf{R}_\alpha^{(s)} + \nu l_\beta \mathbf{u}_\beta|}} \frac{e^{iK(\omega)|\mathbf{R}_\alpha^{(rec)} - \nu l_\beta \mathbf{u}_\beta|}}{\sqrt{|\mathbf{R}_\alpha^{(rec)} - \nu l_\beta \mathbf{u}_\beta|}} d\nu, \quad (22)$$

wherein $\mathbf{R}_\alpha^{(s)} \equiv -\mathbf{x}_\alpha^{(s)} + \mathbf{a}_\beta$ and $\mathbf{R}_\alpha^{(rec)} \equiv \mathbf{x}_\alpha^{(rec)} - \mathbf{a}_\beta$. Since one may picture large curved or flat reflectors as a collection of contiguous small reflectors let us make the following approximations $l_\beta / R_\alpha^{(s)} \ll 1$ and $l_\beta / R_\alpha^{(rec)} \ll 1$. Consequently, one obtains

$$|\mathbf{R}_\alpha^{(s)} + \nu l_\beta \mathbf{u}_\beta| \simeq R_\alpha^{(s)} + \nu l_\beta \mathbf{u}_\beta \cdot \mathbf{w}_\alpha^{(s)}, \quad (23)$$

and

$$|\mathbf{R}_\alpha^{(rec)} - \nu l_\beta \mathbf{u}_\beta| \simeq R_\alpha^{(rec)} - \nu l_\beta \mathbf{u}_\beta \cdot \mathbf{w}_\alpha^{(rec)}, \quad (24)$$

where $R_\alpha^{(s)} \equiv |\mathbf{R}_\alpha^{(s)}|$, $R_\alpha^{(rec)} \equiv |\mathbf{R}_\alpha^{(rec)}|$, $\mathbf{w}_\alpha^{(s)} \equiv \mathbf{R}_\alpha^{(s)} / R_\alpha^{(s)}$, and $\mathbf{w}_\alpha^{(rec)} \equiv \mathbf{R}_\alpha^{(rec)} / R_\alpha^{(rec)}$. Substituting Eq. (23) and Eq. (24) into Eq. (22) yields the following sensitivity kernels

$$G_{c\beta}(\omega) = \frac{i\omega}{8\pi c} \frac{e^{iK(\omega)R_\alpha^{(s)}}}{\sqrt{R_\alpha^{(s)}}} \frac{e^{iK(\omega)R_\alpha^{(rec)}}}{\sqrt{R_\alpha^{(rec)}}} \operatorname{sinc}\left(\frac{K(\omega)l_\beta}{2} [\mathbf{u}_\beta \cdot (\mathbf{w}_\alpha^{(s)} - \mathbf{w}_\alpha^{(rec)})]\right). \quad (25)$$

Evidently, when the approximate result, Eq. (25), and the integral, Eq. (22), coincide and reduce to the point-scatterer result. The final expression, Eq. (25), may also be written in terms the unit vector, \mathbf{n}_β , normal to the line-segment as

$$G_{\alpha\beta}(\omega) = \frac{i\omega}{8\pi c} \frac{e^{iK(\omega)R_\alpha^{(s)}}}{\sqrt{R_\alpha^{(s)}}} \frac{e^{iK(\omega)R_\alpha^{(rec)}}}{\sqrt{R_\alpha^{(rec)}}} \operatorname{sinc}\left(\frac{K(\omega)l_\beta}{2} \left| \mathbf{n}_\beta \times (\mathbf{w}_\alpha^{(s)} - \mathbf{w}_\alpha^{(rec)}) \right| \right). \quad (26)$$

Note the presence of the extra sinc-function terms in the expressions of the sensitivity kernels given by Eq. (26) as opposed to the isotropic point-scatterer case sensitivity kernels. Because of the sinc function, as the scale of the scatterer approaches a wavelength, the scattered field becomes more specular. Thus, the field configurations tend toward the patterns expected in the limiting case of a large thin diffractor where most of the energy undergoes either a specular reflection or a direct transmission. (Recall that our scatterers are only thin inclusions, hence refraction cannot take place).

Appendix B. Homogeneous isotropic backgrounds

In this appendix, we calculate the sensitivity kernels associated with 2D scattering elements in a 3D homogeneous and isotropic medium. The results are used to plot the normalized amplitudes of the sensitivity kernels associated with density contrast $\Delta\rho$, and Lamé parameters $\Delta\lambda$, $\Delta\mu$ in Figs. 4, 5, and 6.

Green’s dyadic for a homogeneous, isotropic medium is given by (Ben-Menahem and Singh, 1981; Snieder, 2002)

$$\mathcal{G}(\mathbf{x}, \mathbf{x}') = \frac{ik_\alpha}{12\pi(\lambda + 2\mu)} \left[\mathbf{I} h_0^{(1)}(k_\alpha \|\mathbf{x} - \mathbf{x}'\|) + \left(\mathbf{I} - 3 \frac{(\mathbf{x} - \mathbf{x}')(\mathbf{x} - \mathbf{x}')^T}{\|\mathbf{x} - \mathbf{x}'\|^2} \right) h_2^{(1)}(k_\alpha \|\mathbf{x} - \mathbf{x}'\|) \right] - \frac{ik_\beta}{12\pi\mu} \left[-2\mathbf{I} h_0^{(1)}(k_\beta \|\mathbf{x} - \mathbf{x}'\|) + \left(\mathbf{I} - 3 \frac{(\mathbf{x} - \mathbf{x}')(\mathbf{x} - \mathbf{x}')^T}{\|\mathbf{x} - \mathbf{x}'\|^2} \right) h_2^{(1)}(k_\beta \|\mathbf{x} - \mathbf{x}'\|) \right], \quad (27)$$

where λ and μ are the usual Lamé parameters, $k_\alpha \equiv \omega \sqrt{\rho / (\lambda + 2\mu)}$, $k_\beta \equiv \omega \sqrt{\rho / \mu}$, and $h_0^{(1)}(\cdot)$ and $h_2^{(1)}(\cdot)$ are the spherical Hankel functions of the first kind.

For such a medium the contrasts in the stiffness coefficients are given by

$$\Delta c_{nkij} = \Delta\lambda \delta_{nk} \delta_{ij} + \Delta\mu (\delta_{ni} \delta_{kj} + \delta_{nj} \delta_{ki}) \quad (28)$$

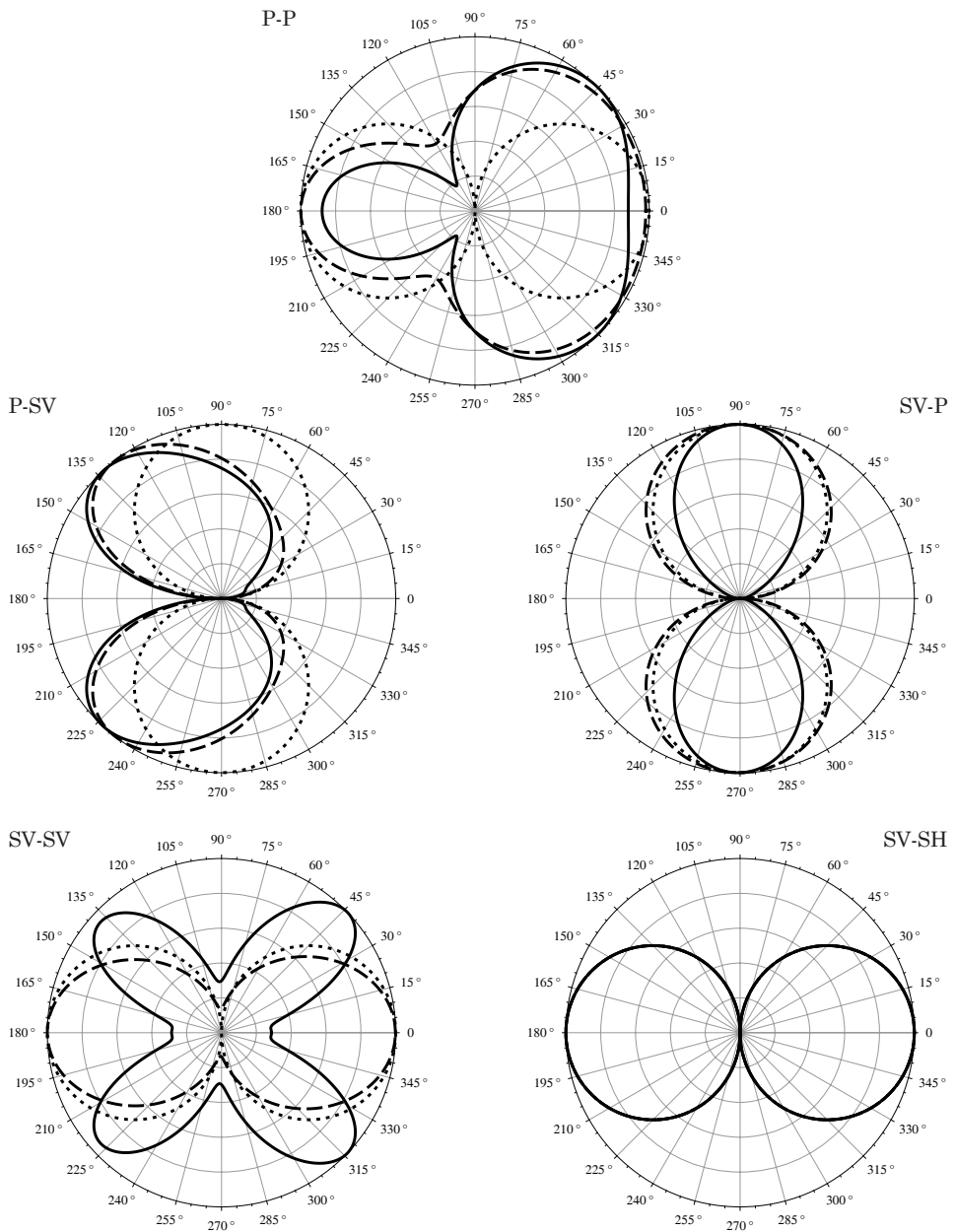


Figure 4. Polar plots of the normalized sensitivity-kernel amplitudes associated with density contrast $\Delta\rho$. The setup consists of one source-receiver pair and one scattering disk of radius r . The plots are all in the xy -plane except for the SV-SH plots which are in the yz -plane. The dotted curves correspond to $2r = 0.02$ wavelengths, the dashed curves correspond to $2r = 0.6$ wavelengths, and the continuous curves correspond to $2r = 1.2$ wavelengths.

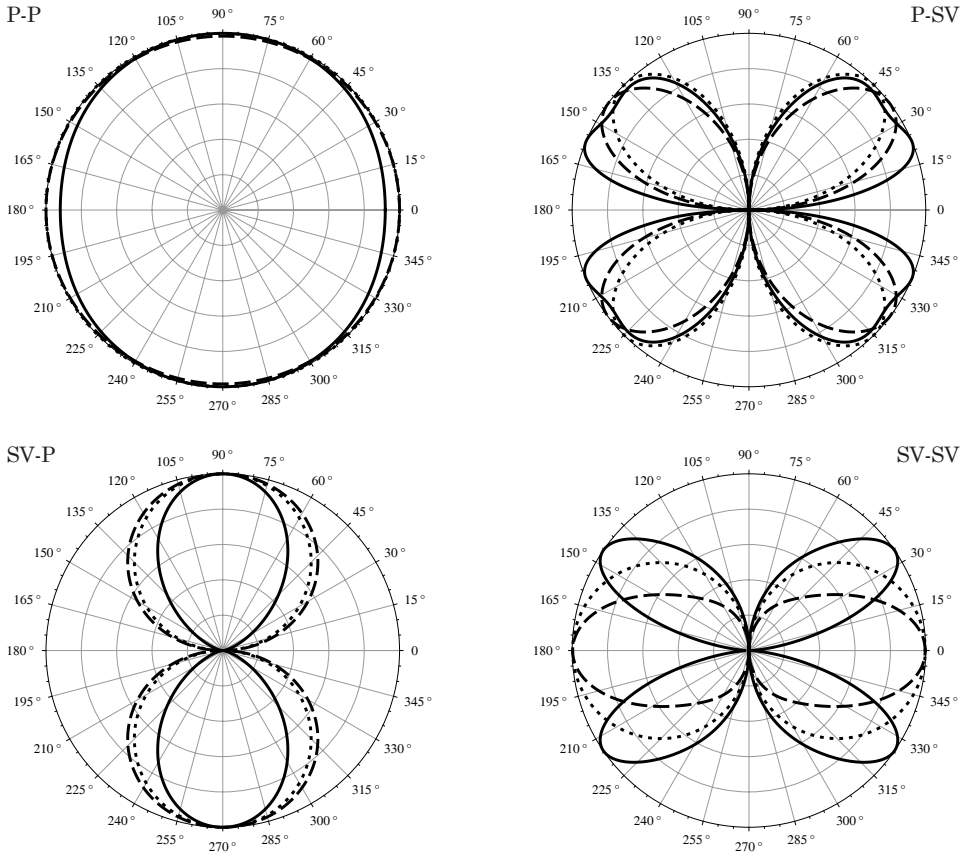


Figure 5. Polar plots of the normalized sensitivity-kernel amplitudes associated with the Lamé parameter contrast $\Delta\lambda$. Note the absence of SV-SH plots. The setting is the same as that of Fig. 4.

Let us consider the simple case of a single scattering element which is assumed to be a disk of radius r . Substituting Eqs. (27) and (28) into Eq. (11) yields the following sensitivity kernels

$$G^{(\rho)} = \omega^2 \int_{\mathcal{A}^{(2)}} \sum_{i,j} \mathcal{G}_{ij}^{(0)}(\mathbf{x}, \mathbf{y}(\Lambda^{(2)}), \omega) \wp_i^{(sca)} \sum_m \mathcal{G}_{jm}^{(0)}(\mathbf{y}(\Lambda^{(2)}), \omega) \wp_m^{(inc)} d\Lambda^{(2)} \quad (29)$$

$$G^{(\lambda)} = - \int_{\mathcal{A}^{(2)}} \left[\sum_{i,n} \partial'_n \mathcal{G}_{in}^{(0)}(\mathbf{x}, \mathbf{x}', \omega) \wp_i^{(sca)} \sum_{j,m} \partial'_j \mathcal{G}_{jm}^{(0)}(\mathbf{x}', \omega) \wp_m^{(inc)} \right]_{\mathbf{x}'=\mathbf{y}(\Lambda^{(2)})} d\Lambda^{(2)} \quad (30)$$

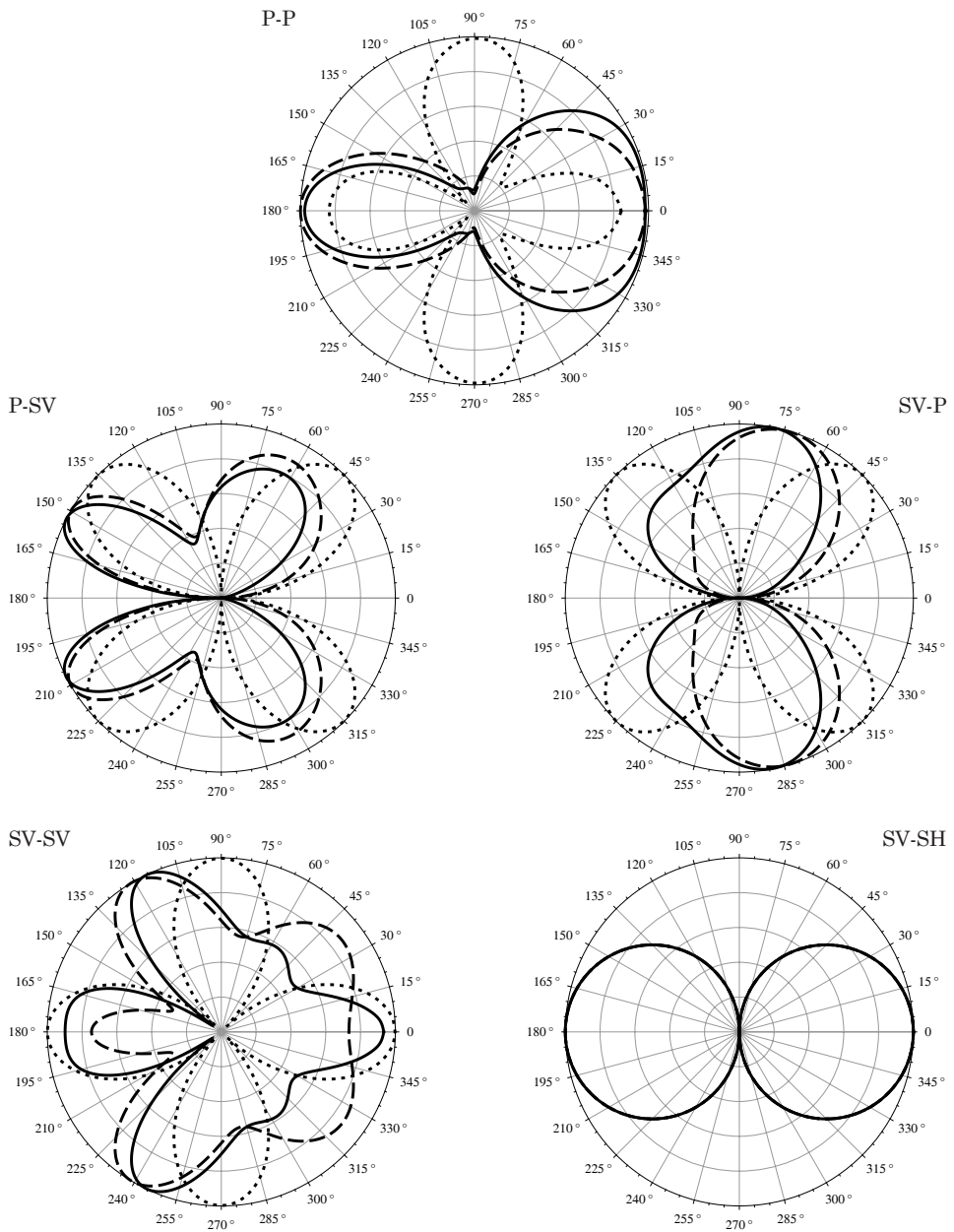


Figure 6. Polar plots of the normalized sensitivity-kernel amplitudes associated with the Lamé parameter contrast $\Delta\mu$. The setting is the same as that of Fig. 4.

$$G^{(\mu)} = - \int_{\mathcal{A}^{(2)}} \left[\sum_{i,j,n} \partial'_j \mathcal{G}_{in}^{(0)}(\mathbf{x}, \mathbf{x}', \omega) \wp_i^{(sca)} \times \right. \\ \left. \times \sum_m \left(\partial'_j \mathcal{G}_{nm}^{(0)}(\mathbf{x}', \omega) + \partial'_n \mathcal{G}_{jm}^{(0)}(\mathbf{x}', \omega) \right) \wp_m^{(inc)} \right]_{\mathbf{x}'=\mathbf{y}(\Lambda^{(2)})} d\Lambda^{(2)}, \quad (31)$$

where we have introduced the unit incident-wave polarization vector $\wp^{(inc)}$ and the unit scattered-wave polarization vector $\wp^{(sca)}$. In the examples presented here, the setup consists of one source-receiver pair and one scattering disk of radius r located at the origin of coordinates and oriented in such a way that the x -axis is perpendicular to its plane. The source is assumed to be located on the x -axis to the left of the scattering disk. The receiver is assumed to be in the far zone. For simplicity the polarization vectors were taken to be

$$\wp_P^{(inc)} = (1, 0, 0)^T \quad (32)$$

$$\wp_P^{(sca)} = \mathbf{x}^{(rec)} \equiv \frac{1}{\|\mathbf{x}^{(rec)}\|} (x, y, 0)^T \quad (33)$$

$$\wp_{SV}^{(inc)} = (0, 1, 0)^T \quad (34)$$

$$\wp_{SV}^{(sca)} = \frac{1}{\|\mathbf{x}^{(rec)}\|} (y, -x, 0)^T \quad (35)$$

$$\wp_{SH}^{(sca)} = (1, 0, 0)^T \quad (36)$$

Consequently, the plots are all in the xy -plane except for the SV-SH scattering plots which are in the yz -plane. The results are shown in Figs. 4, 5, and 6. The absence of SV-SH plots in Fig. 5 is due to the vanishing of the energy scattered in the yz -plane in the case of a purely tensile contrast. Clearly, the anisotropy radiation patterns can significantly differ when accounting for the size of the scatterer.

